Tribology Letters, Vol. 26, No. 2, May 2007 (© 2007)
DOI: 10.1007/s11249-006-9125-5

A multi-technique characterization of ZDDP antiwear films formed on Al (Si) alloy (A383) under various conditions

G. Pereira[a], A. Lachenwitzer[a], M. Kasrai[a], P.R. Norton[a,*], T.W. Capehart[b], T.A. Perry[b], Y.-T. Cheng[b], B. Frazer[c] and P.U.P.A Gilbert[c,d]

[a]*Department of Chemistry, University of Western Ontario, London, Ontario Canada N6A 5B7*
[b]*Materials and Processes Laboratory, General Motors R&D, Warren, MI 48090, USA*
[c]*Physics Department, University of Wisconsin at Madison, Madison, WI 53706, USA*
[d]*University of Wisconsin Synchrotron Radiation Center, Stoughton, WI 53589, USA*

Received 29 July 2005; accepted 13 November 2005; published online 23 February 2007

The simulation of the lubrication of aluminum–silicon (Al–Si) alloy cylinder-bore conditions is an important goal in automotive tribology. This study describes the use of X-ray absorption near edge structure (XANES) to determine the macro-chemistry of zinc-dialkyl-dithiophosphates (ZDDPs) antiwear (AW) films formed on A383, an Al-Si alloy. The temperature dependence of the chemistry and mechanical properties were examined using X-ray photoelectron emission microscopy (X-PEEM), and imaging indentation techniques. Our findings suggest that ZDDPs break down to form polyphosphate glasses, which have different chemical natures and depend on the underlying substrate. Furthermore, the chemical nature of the films appears temperature dependent on both the macro- and micro-scale. Not only are the chemical species different, but the mechanical properties also differ, depending on the region upon which an AW pad is formed. Through the use of focused ion beam (FIB) milling, we can determine the film thickness, which was previously estimated from the P K-edge XANES areal density of samples with known thicknesses.

KEY WORDS: ZDDP, XANES, X-PEEM, FIB, SEM-EDX, nanoindentation, polyphosphate, mechanical properties, tribofilm

1. Introduction

Aluminum–silicon (Al–Si) alloys constitute a class of material that are being used to replace cast iron parts in automobile engines. Benefits of the replacement to the car industries include resistance to corrosion, good thermal conductivity, and moderate costs. Aluminum is used specifically to reduce weight compared to steel, and is alloyed with silicon to increase the strength of the material. It is well known that silicon solidifies in a separate hard phase, which becomes the load-bearing surface.

The first cylinder block used with an Al/Si liner was used by General Motors (GM) in the Chevrolet Vega engine [1,2]. The bore was electrochemically etched to expose the primary Si grains on the surface. Experience showed that bores that were not etched resulted in cold-scuff failures, and when over etched, resulted in high-piston wear and ring wear, most likely due to over exposure of the Si grains that become dislodged in the etching process, generating many hard third bodies [2]. The Chevrolet Vega was discontinued at the end of the 1977 model year, and GM resorted back to the traditional steel liners. However, the motivation to reduce vehicle weight and increasingly restrictive environmental legislation, has led to Al–Si alloys being considered again to replace cast iron and steel in engines.

Much previous work has focused on the dry-sliding of Al–Si alloys [3–6], and very little on the lubrication of these alloys [7–11]. It is well known that the steel/aluminum couple is a difficult system to lubricate even at modest loads [7,10], and furthermore that additives added to formulated oils that protect steel and cast iron surfaces, do so by forming protective films [12,13].

The most widely studied lubricant additives, due to their antiwear (AW) and antioxidant performance are the zinc dialkyl-dithiophosphates (ZDDPs) which have been the subject of recent review articles [12–15]. ZDDPs are a class of engine oil additive that work in conjunction with other objective-specific additives (i.e., friction modifiers, detergents, dispersants). In boundary lubrication, ZDDPs are capable of forming an amorphous protective solid film (AW film, tribofilm), which prevents direct contact of the rubbing metals [13,16,17]. The AW action of the AW films, which are composed of polyphosphates of varying chain length, has been attributed to the resiliency of the films, as the film bears the load between the surfaces in contact, thereby reducing wear.

Recently, Hershberger *et al.* [18] using very high-ZDDP concentrations has provided insight about the role of the Zn cation in the formation of polyphosphate glasses. It was shown that with X-ray fluorescence

---

*To whom correspondence should be addressed.
E-mail: pnorton@uwo.ca

that the Zn atom concentrations in the thermal films are distinctly higher than for tribologically prepared samples, and furthermore an atomic concentration threshold was found for the Zn atoms in the films based upon the ZDDP concentration. The cation composition in the polyphosphate films is dependent on the available sources. Much early work has shown that when ZDDP is the only additive studied, Zn is the cation principally associated with the polyphosphate [19–22].

Hsu and Gates [17] briefly explains the importance of the dual role of the mechanical properties of thin AW ZDDP-derived films. AW films must be both hard and capable of bearing a load under high-stress conditions, but must also behave as a softer, shearable material. This dual action of the film is required to distribute the contact forces in order to prevent damage to the surface it is protecting.

These films have recently been studied by imaging nanoindentation and have exhibited unique mechanical properties [16,23–25]. The indentation moduli of the films formed on steel surfaces were found to vary with location and size of the pads. Nicholls *et al.* [24] found values for E_s^* ranging of ~81.0 GPa for AW pad ridges and ~25.0 GPa for AW pad valleys for films formed on steel. Graham *et al.* [26] reported an indentation modulus as high as 209 ± 38 GPa in the center of large pads. Nicholls *et al.* [27] and Pereira *et al.* [11] reported E_s^* values ranging ~77 GPa for the tribofilm on different Al–Si alloys. Al–Si alloy surfaces are more complex than steel surfaces in the sense that the underlying microstructure seems to play a role in the mechanical response of the AW film [11].

Although these films have been extensively studied through a variety of techniques (mainly on steel surfaces), the formation, specific location, and structure of the AW films are still only partially known. Various surface analysis techniques have been employed to elucidate and characterize tribofilm formation: e.g., AES, XPS, ToF-SIMS, X-ray absorption near edge structure (XANES), and X-ray photoemission electron microscopy (X-PEEM). Arguably, XANES is the most sensitive analytical tool for our branch of studies. Oxidation state and degree of polymerization of the absorbing atom can be obtained by comparing the spectra with those of model compounds. X-PEEM permits XANES spectra to be obtained with ~100–200 nm lateral resolution [28–30], providing elemental and chemical information at this length scale. XANES spectra of the energy specific absorbing atom can be obtained and corresponding images can be recorded at incremental photon energies.

X-PEEM has found wide-ranging applications in biology, medicine, geology, archaeology, and materials science [29,31] and has already been applied to study many tribological systems. Canning *et al.* [32] was the first to use X-PEEM to study tribological films formed on steel, which eventually led to correlated nanoscale chemical and mechanical characterization of AW films formed on steel. Different chemical species (ZDDP and phosphate) can be readily imaged and selected features correlated to the substrate [11,23,25]. X-PEEM has allowed us recently to show that effective AW films, which consist of longer chain-length polyphosphate glasses, develop selectively on the silicon grains on a near hypereutectic Al–Si alloy [11].

Atomic Force Microscopy (AFM) can provide detailed topographical information on the tribofilms. This information, obtained at ambient temperature, represents a steady-state "snapshot" of the surface at the end of the rubbing experiment, which we utilize to develop an understanding of the film formation. The mechanical properties of the same region can then be determined by imaging nanoindentation.

Understanding the friction characteristics of ZDDPs used to lubricate novel materials is important in order to assess the level of interaction between the two rubbed materials. The coefficient of friction (μ) is a value found to be material and condition dependent [33]. Numerous friction studies involving engine oil additives are presented in literature [34–36]. For very light loads, the friction is controlled by elastic contacts of the asperities and viscous drag of the lubricating oil [37].

The aim of this study is to investigate how the tribofilm forms under several conditions using a multi-technique approach on an Al–Si alloy, which is under consideration for use in cylinder bores, and other engine components.

2. Experimental

2.1. Sample preparation

Cylinder bores of the aluminum alloy, A383 [38] (~0.10% Mg, ~0.15% Sn, ~0.30% Ni, ~0.50% Mn, ~1.3% Fe, ~2.5% Cu, ~3.0% Zn, ~10.5% Si) were prepared at the GM Research and Development Foundry (Warren, MI, USA) and were cut with a wire electric discharge machine (EDM) into square disks with dimensions of $12 \times 12 \times 4$ mm^3 (± 0.5 mm). The disks were mechanically polished with 600 and 1200 grit SiC paper and subsequently polished with 0.6, 0.3, and finally 0.05 μm alumina pastes. The disks were then washed in methanol in an ultrasonic bath and stored in air to dry.

2.2. Morphology and topography data acquisition

Atomic force microscopy topography images were compiled for all the samples in air, using a Nanoscope IIIa equipped with a Multimode™ head (Digital Instruments, Santa Barbara, CA, USA). The images were collected in contact force mode with a V-shaped silicon nitride cantilever possessing a nominal spring constant of 0.12 N/m.

The SEM/mapping EDX data were collected at Surface Science Western, located at the University of Western Ontario, using a Hitachi S4500 SEM equipped with an EDAX™ light element EDX microanalysis system. The images presented were acquired with a 5 kV acceleration electron beam voltage, a 17 mm working distance, and a 30° tilt in the field emission mode.

2.3. Antiwear film preparation and characterization

Commercial ZDDP consisting of secondary butyl groups (85%) and n-octyl groups (15%) in MCT-10 base oil were obtained from Imperial Oil (ESSO) of Canada. ZDDP solutions were prepared by mixing ZDDP concentrate in MCT-10 base oil.

Antiwear films were made on A383 using steel pins in a Plint high-frequency friction machine. The A383 disks and cylindrical 52100 steel pins were cleaned in an ultrasonic bath using a light hydrocarbon solvent, and then placed in the Plint high-frequency wear tester. The ZDDP solution was placed in the Plint wear tester and the steel pin was laid flat against the disk (cylindrical face in contact with the surface). The normal applied load was 40 N [calculated maximum contact pressure after experiment ranged from 5 –to 45 MPa, which depends on the wear scar width (WSW)]. The software monitored the temperature and lateral force (F_T) throughout the experiment. The coefficient of friction (μ) is a calculated ratio between F_T and the normal force (F_N) given by equation (1);

$$\mu = \frac{F_T}{F_N}. \tag{1}$$

We present the coefficient of friction (μ) values as a measure of relative interaction of the rubbed surfaces.

The influence of various experimental parameters was studied independently, changing one variable at one time (table 1). Parameters such as load, frequency, rubbing time, temperature, and ZDDP concentrations were tested. After each experiment, excess oil was removed from the disks using tissue paper and then the samples were rinsed in hexane.

A grid consisting of indented marks was created using a Vickers hardness tester using loads of 100 and 500 g, which made indents ~25 and ~100 μm across, respectively. The distance between the indents was ~100 μm and the larger indents were used to generate identifiable features for easy relocation.

Table 1.
Variation of the physical parameters studied. AW films were made under lubrication conditions outlined in the text on the A383 substrate. All parameters were studied independently changing one variable at a time.

Experimental variables	Conditions
Load (N)	15, 25, 40
Time (min)	5, 30, 720
Frequency (Hz)	15, 25, 40
Temperature (°C)	60, 100, 150
ZDDP concentration in MCT-10 base oil (%)	0.3, 0.6, 1.2, 2, 100

The grid allowed for relocation of the same region with multiple techniques. The wear tests were made in duplicate.

2.4. XANES Spectroscopy and X-PEEM Spectromicroscopy data acquisition

XANES data were obtained at the Canadian Synchrotron Radiation Facility (CSRF) [39], situated at the 1 GeV Aladdin storage ring, University of Wisconsin, Madison, USA. Phosphorus, and sulfur K-edge XANES spectra were obtained on the double-crystal monochromator (DCM) [40] covering an energy range of 1500–4000 eV with photon resolution of 0.8 eV. Phosphorus, and sulfur L-edge XANES spectra were obtained on the Grasshopper soft X-ray beamline covering an energy range of 70–900 eV with photon resolution of 0.2 eV at the phosphorus L-edge. The energy scales for the phosphorus K- and L-edges were calibrated using pure ZDDP [19]. The energy scale for sulfur K- and L-edges was calibrated using ZnS and FeS_2 [19,41,42]. The analyzed area was about 2×2 mm^2. The photoabsorption spectra for both the model compounds and samples were recorded in the total electron yield (TEY) mode and fluorescence yield (FY) mode for both surface and bulk sensitivity [43]. All spectra shown in this paper are an average of three scans that were digitally combined and normalized, with a linear background subtracted using the BAN program (T. Tyliszczak, unpublished data). The assignment of the fine structure in XANES was carried out using model compounds obtained by the authors or by comparison to previous results.

Peak fitting was performed to provide semi-quantitative results for the amount of each, phosphorus and sulfur species, present in the wear scar. Phosphorus and sulfur K- and L-edge spectra were fitted using the BGAUSS program (T. Tyliszczak, unpublished data). Peaks were fitted using a Gaussian line and specific constraints to the element's absorption edge, similar to previous efforts [7]. An arctangent step function representing the transition of ejected photoelectrons to the continuum has been fitted to the spectra. The peak widths and positions for the spin-orbit splitting were fixed to be equal. The decay of the arctangent was also fixed for each fit. All other parameters were allowed to vary. In some instances, the Gaussian peaks representative of the phosphorus and sulfur species were fixed to specific energy positions close to what was expected for the particular species. The relative fraction of each species was calculated by determining the area of the Gaussian peak for that species divided by the total area of all the Gaussian peaks for each phosphorus species present in the wear scar. These fractions of the phosphorus species were then compared to calibrated polyphosphate compounds with known chain lengths whose peaks have been fitted in the same manner.

X-PEEM was performed using the SPHINX [31] microscope (ELMITEC GmbH) installed on the HERMON beamline using the low-energy grating ranging between 62 and 144 eV at the 1 GeV Aladdin storage ring, University of Wisconsin, Madison, optimized to give ~0.2 eV resolution at the phosphorus L-edge (for details see Refs. [23,31,44]). Image intensity in X-PEEM is proportional to the TEY and the surface sensitivity was limited by the escape depth of the secondary electrons at the phosphorus L-edge (3–5 nm) [44,45]. Spectromicroscopy images were taken with a 0.2 eV step size from high energy to low energy. A 100-μm field of view was chosen for the selected area with a resolution of ~200 nm per pixel. The images were combined to produce a three-dimensional data set or spectromicroscopy 'stack' [46] that was analyzed to extract detailed chemical information about the tribofilm using aXis2000 software [46,47]. The software allowed for selection of regions of several pixels in size to extract XANES spectra. Stacks were acquired at the phosphorus L-edge (130–144 eV) and analyzed for differences in chemistry.

Unfortunately, the low-energy grating of the beamline limited the remaining elements to be collected in second order (Bragg equation). Signals acquired at the aluminum (70–90 eV) and silicon (90–130 eV) L-edges, but were generally noisy and too weak to obtain meaningful spectra.

Rectangular cross-sections of the AW films studied by X-PEEM were excised with a focused ion beam (FIB) installed on a LEO 1540XB scanning electron microscope at the Nanofabrication Laboratory, at The University of Western Ontario. The ions used for machining were gallium (Ga^+) with a current of 50 pA for 300 s. The AW film thickness was averaged along the cut. Imaging with the SEM was done prior to and after the FIB milling.

2.5. Nanomechanical property and wear performance

The mechanical properties of the substrate and AW films were investigated using a Hysitron Triboscope®. This system has the capability to produce topographic images of a surface directly before and after indenting, using the force transducer. Details of the specific instrumentation and setup are given elsewhere [24]. An AFM J-scanner was used to image the surface. The three-sided diamond Berkovich indenter with an elastic modulus (E_i) between 1000-1140 GPa, a Poisson ratio (v_i) of 0.07 and a tip radius of curvature between 110 and 130 nm was used for all indentations. Topographic images were taken before and after indenting a region. A certain preset force was applied and the resulting depth of penetration of the indenter is recorded. Both the loading of the preset force and unloading was monitored. The elastic modulus was extracted using the Oliver–Pharr method [48] from the unloading section of the force–distance (f–d) curve. The range of applied loads studied was 30–300 μN.

The WSW of the steel pins was measured using a calibrated optical Zeiss Axioplan microscope over 10 random regions along the length of the pin. The values of the WSW are used as a measure of wear performance.

3. Results and discussion

3.1. Macro-chemistry of the tribofilms

Figure 1 compares three tribofilms (A–C—table 2) analyzed using the phosphorus L-edge. The L-edge for phosphorus probes electronic transitions from the 2p orbitals to unoccupied higher level s and d orbitals [19]. To help elucidate the chemistry of the film, we compare the spectra of the films with those of model compounds of known structure and geometry. The L-edge spectra provide results that is appreciably more surface sensitive (better resolution), and better detailed [45] than the P K-edge. The L-edge and P K-edge spectra (see below), are consistent with previous studies of boundary lubri-

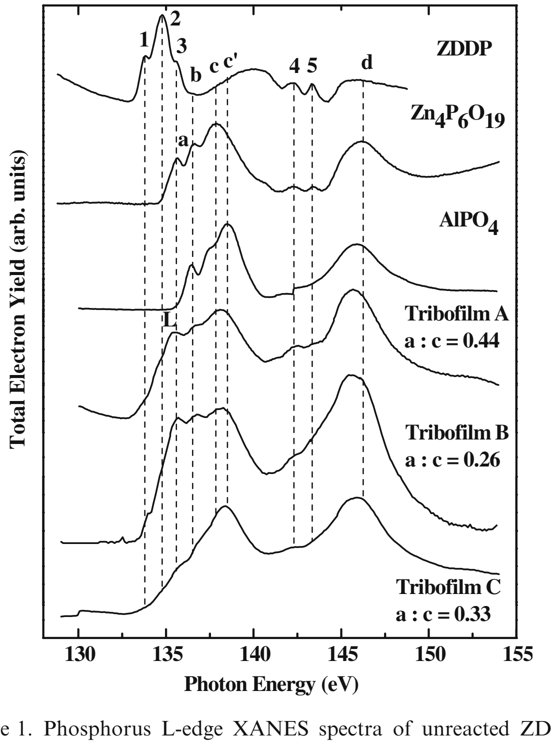

Figure 1. Phosphorus L-edge XANES spectra of unreacted ZDDP, model compounds $Zn_4P_6O_{19}$ and $AlPO_4$, and three tribofilms. The conditions under which tribofilms A–C were made are shown in table 2. Tribofilm A was made under 40 N, 25 Hz, 30 min, 1.2% ZDDP, and 100 °C. Tribofilm B was made at 200 °C, and tribofilm C was rubbed for 720 min.

Table 2.
Tabulated experimental parameters, whose spectra is presented.

Tribofilm A	40 N, 30 min, 25 Hz, 100 °C, 1.2% ZDDP
Tribofilm B	40 N, 30 min, 25 Hz, 150 °C, 1.2% ZDDP
Tribofilm C	40 N, 30 min, 25 Hz, 100 °C, 0.3% ZDDP

cation of steel pins on steel surfaces, and other Al–Si alloys, in showing that the shift of the tribofilm peaks compared to those in ZDDP, are consistent with the formation of a polyphosphate glass [7,11,49–51].

The shoulder on the low-energy side of the peak labeled ‘a’ of the tribofilms has been identified as originating from unreacted ZDDP (which is aligned with ZDDP’s peak 2); this is also consistent with the P K-edge XANES [7,11,49,51]. All tested conditions showed some indication of unreacted ZDDP. The unreacted ZDDP is most probably embedded or entrapped in grooves and valleys carved by the asperity contacts.

The spectra presented in figure 1 (tribofilm A) closely resemble the spectra obtained by Nicholls *et al.* [7] for the 52100 steel pin rubbing against other Al–Si alloys, both A6061 and A319, and by Pereira *et al.* [11] for the etched Silitec 5™ alloy. The principal difference in the substrates is the silicon content; the Silitec 5 alloy has a higher Si weight percentage, while the A6061 and A319 have lower Si weight percentages than A383.

We immediately notice that peak ‘a’ of $AlPO_4$ is shifted to higher energies compared to that of the tribofilms. Thus, the formation of $AlPO_4$ in the tribofilm is unlikely. The appearance of the peak labeled ‘L’ has been attributed to the formation of an intermediate linkage isomer (LI) of ZDDP [7,50]. Suominen-Fuller *et al.* [50] have observed the formation of the LI in thermally generated films at 150 °C. The authors suggest that LI is an intermediate of the ZDDP decomposition process that eventually decomposes into a polyphosphate. The LI is a rearranged form of ZDDP in which an alkyl group has transferred from an oxygen atom to a sulfur atom. This rearrangement results in a higher formal charge on the P atom, causing a shift to higher energy [50]. An LI has been observed on certain AW films formed on other Al–Si alloys after rubbing [7,9], although most work has been done at lower temperatures.

Yin *et al.* [52] have shown that the ratio of intensities of peaks a : c and b : c increases with increasing polyphosphate chain length. Nicholls *et al.* [23] have provided a calibration curve assigning the a : c intensity ratios from the P L-edge. We have previously [11] assigned short chain polyphosphates to have 10 or fewer P atoms in a polyphosphate glass corresponding to an a : c ratio of ~0.44 or less. Long chain polyphosphate species (defined as chains containing 35 or more P atoms), result in an a : c ratio of ~0.60 or greater. Medium to short chained polyphosphates therefore are characterized by an a : c ratio between ~0.44 and ~0.60, and consist of chains containing between 10 and 25 P atoms.

A peak fitting procedure was used to estimate the polyphosphate chain length of the tribofilms. An example of peak fitting is shown in figure 2 for tribofilm B. Three peaks were assigned for ZDDP (for details of assignment see Refs. [19,23,24,53]), and another three peaks were assigned for the LI initially at ~135.6 eV with the same shifts as for ZDDP. The polyphosphate glass was fit with four peaks and an arctangent background was subtracted. The deconvoluted area of peak a relative to peak c was found to be 0.26, implying a short chain polyphosphate network. The spectra shown in figure 1 indicate that tribofilm A (a : c ≈ 0.44) is a short to medium chain or network of polyphosphates, and tribofilm c is made of short networks of polyphosphates (a : c ≈ 0.33).

Previously, Yin *et al.* [51] have suggested that ZDDP decomposes much faster on steel coupons rubbed by steel pins at elevated temperatures and generates shorter chains of polyphosphates when compared to lower or ambient temperatures (other parameters remaining constant). The intensity of pre-peak shoulders for the tribofilms (which align with peaks 1 and 2 of ZDDP) are decreased at higher temperatures, supporting the findings on steel [51] and also on other Al/Si alloys [54].

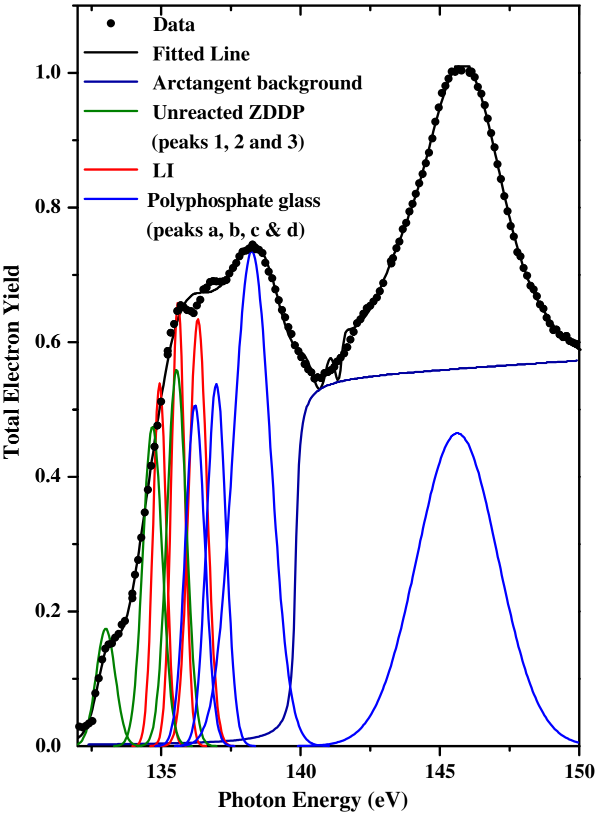

Figure 2. An example of peak fitting performed on the P L-edge XANES data to determine the polyphosphate chain length. This example is for tribofilm B. Peaks were fit for unreacted ZDDP, the LI, and the polyphosphate glass. The peak at ~135.6 eV originates from the LI, fit in the same manner as ZDDP (see text for details).

In the same report, Yin *et al.* [51] have used P L-edge XANES to compare the effects of the concentration of ZDDP on the formation of various species on steel surfaces. Our results provide evidence that un-reacted ZDDP (which aligns with peak 2 (figure 1)) decreases significantly when the concentration of ZDDP is decreased from 1.2 to 0.3%. Current U.S. environmental laws regulate maximum P content in passenger vehicles to 0.1%, resulting in a ZDDP concentration of ~1% [18], which has also been found to be close to the optimum ZDDP concentration range for the AW regime [55]. Chao *et al.* [55] has suggested that increasing ZDDP concentrations promote thicker films, which are also formed more rapidly. In addition, he suggested that lower concentrations of ZDDP will lead to significantly less adsorption on the surface, resulting in the formation of shorter chain polyphosphates. The data in figure 1 are in agreement with both findings.

Figures 3 and 4 show the phosphorus K-edge spectra collected in the TEY mode for the tribofilms on A383. Figure 3 shows three tribofilms prepared under different conditions (table 2). The spectra are characteristic of typical P K-edge XANES spectra for phosphates. The explanation of the absorption features has been described elsewhere [24]. There is a discernible shift in the main peak from ZDDP (peak a) compared to any of the main peaks of the model compounds (peaks b and c). The shift between peak a (ZDDP) and peak b and c (model phosphates) are attributed to the environment of the absorbing P atom. In ZDDP, the P atom is coordinated to two sulfur atoms and two oxygen atoms, whereas in phosphate, the P atom is coordinated to four oxygen atoms, causing the observed shift in absorption energy, as previously described [24]. This is evidence that the P atoms in the tribofilms have a different chemical environment compared to that of unreacted ZDDP, and chemically resemble the phosphate model compounds. The shift between the model zinc phosphate ($Zn_4P_6O_{19}$) and the model aluminum phosphate ($AlPO_4$) is attributed to the strength the cation has on shielding the core P atoms in excitation [19]. The shoulder labeled 'a' on the tribofilms is evidence that unreacted ZDDP is present which is in agreement with the P L-edge findings.

Peak fitting was performed to provide semi-quantitative results for the amount of phosphorus species present as either unreacted ZDDP or phosphate in the wear scar. An example of peak fitting is shown in figure 4 for tribofilm A. The discussion of how the peaks were fit is given elsewhere [7]. Briefly, the relative fractions of each P species was calculated by determining the area of the fit Gaussian peak for that species, divided by the total area of all the Gaussian peaks for each P species present in the wear scar. It was found that the percentage of phosphate present in the film was ~83 ± 7% under almost all conditions. High temperatures (150 °C) and long-rubbing times (720 min) generated the most phosphate species (>91%), attributed to the extreme conditions from which these films were made, consistent with results on steel [51].

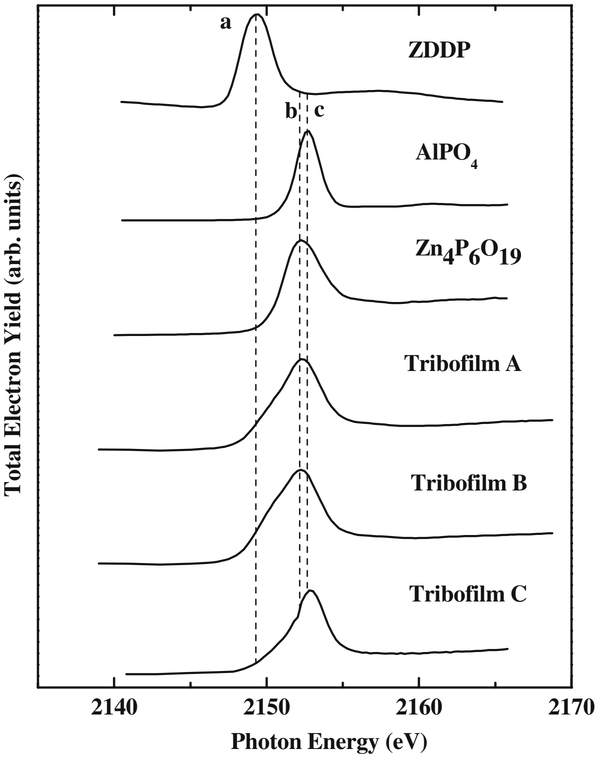

Figure 3. Phosphorus K-edge XANES spectra of unreacted ZDDP, model compounds $AlPO_4$ and $Zn_4P_6O_{19}$, and the tribofilms (table 2) on A383.

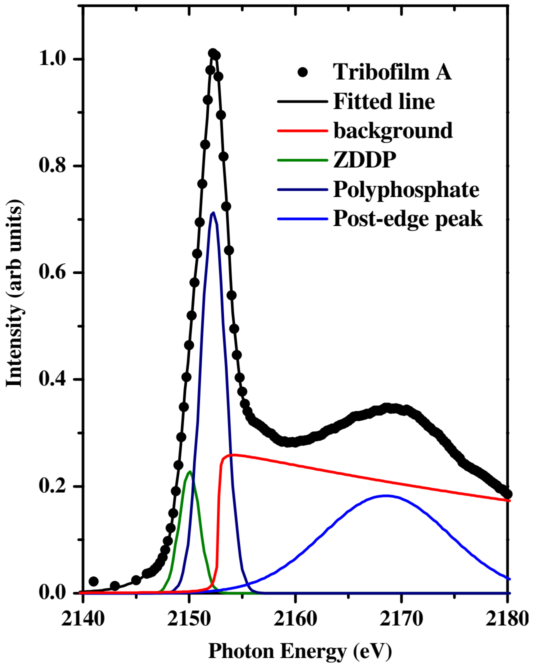

Figure 4. An example of peak fitting performed of the P K-edge data to determine the relative percentage of phosphorus species detected in the wear scar. This example is for tribofilm A (table 2).

Due to the high-sampling depth of the energetic P K-edge photons, the mass thickness of the tribofilms can be determined from the fluorescence intensities calibrated via the particle induced X-ray emission (PIXE) [56]. The thickness can then be estimated from the mass thickness assuming a uniform polyphosphate with stoichiometry $Zn_2P_2O_7$, and a density of 3.75 g/cm^3. From this method, the average film thicknesses for tribofilm A and B were found to be 40 ± 2 and 42 ± 4 nm, respectively.

3.2. *Spatially resolved chemistry of the tribofilms*

X-PEEM measurements were carried out on representative areas of the tribofilm. Through the use of fiducial marks, the same areas were examined using several techniques. Figures 5 and 6 present topographic and chemical maps for tribofilms A and B obtained by AFM, SEM-EDX, and X-PEEM. Figures 5(a, b) and 6(a, b) are 50×50 μm^2 AFM height and deflection images of the respective tribofilms. Markers (labeled A–D) are outlined for future reference. The dashed lines in figures 5(a) and 6(a) are cross-sections in which regions were cut with the FIB, and will be addressed later. The dashed boxes in figures 5(b) and 6(b) are regions that exhibited different mechanical responses, as will be further discussed.

The topography detected in the height image of tribofilm A (figure 5(a)) looks quite uniformly leveled around the cavities shown in the center of the image compared to tribofilms formed on other Al–Si alloys under similar conditions [11]. We do not see large pads (> 10 μm) elongated in the sliding direction as was previously observed from the tribochemical decomposition of ZDDP on steel surfaces [26], consistent with previous studies on other Al–Si alloys [11]. The flatter features surrounding the cavities labeled 'A' and 'B' are better displayed in the deflection images, because topography is suppressed and edges are enhanced showing a 'sharper' image. The deflection images show a uniform patchy region surrounding some very rutted and coarse areas.

Deflection images are displayed because they posses richer contrast compared to their equivalent AFM height images. The morphological differences between the Al–Si alloys are most likely related to how the substrate was prepared and treated. The Silitec 5 alloy (23–26% Si) [11] has a more uniform size and narrow

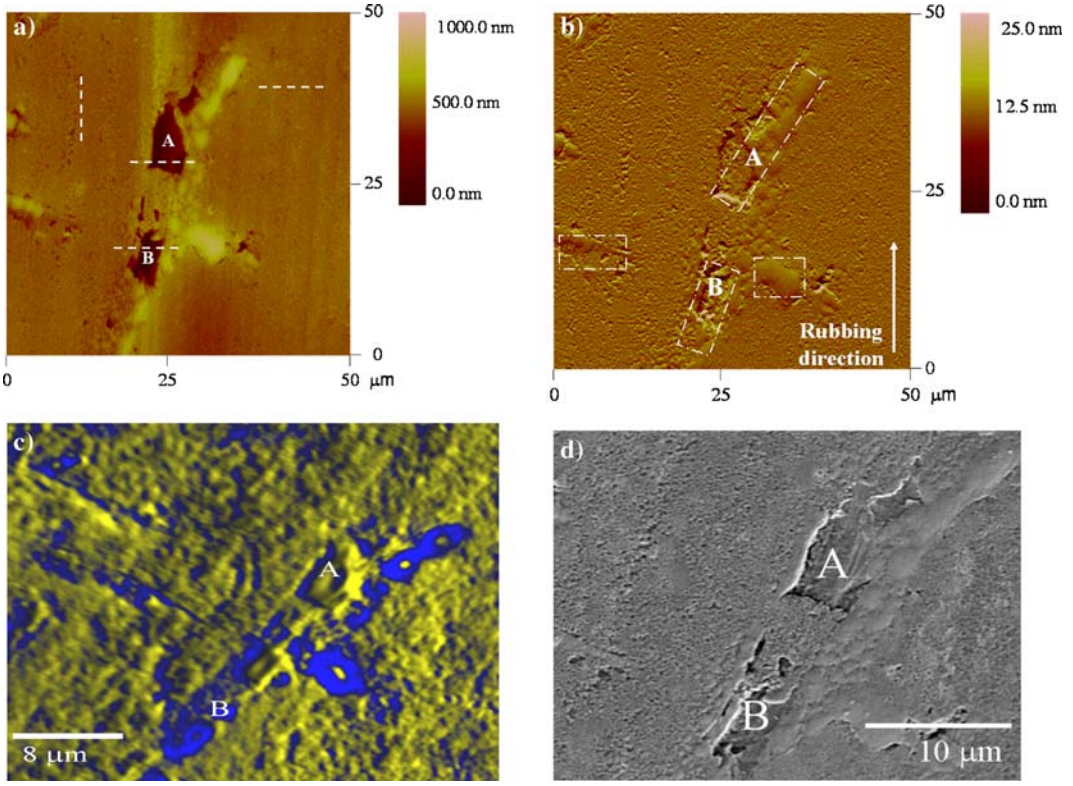

Figure 5. Chemomechanical mapping of tribofilm A. The region shown was analyzed by multiple techniques. Regions of interest are indicated that can be compared throughout the chemomechanical map. Figure 5(a, b) is 50×50 μm^2 contact AFM height and deflection topography images. The dashed lines and boxes are explained in the text. Figure 5(c) is the X-PEEM distribution map of the region analyzed of tribofilm A. The yellow regions indicate short chain polyphosphates and the blue areas represent regions of long chain polyphosphates. Black areas are regions where the spectra were not fitted well with neither long nor short chain polyphosphates. Figure 5(d) A field emission SEM image and figure 5(e, f) mapping EDX of a tribofilm A taken at 5.0 kV and a 17 mm working distance. Brighter areas in the EDX map indicate an abundance of the particular element shown. Figure 5(g) is the corresponding spectra used to generate the maps in this figure and figure 6. The spectra were acquired in regions smaller less than 4 μm^2.

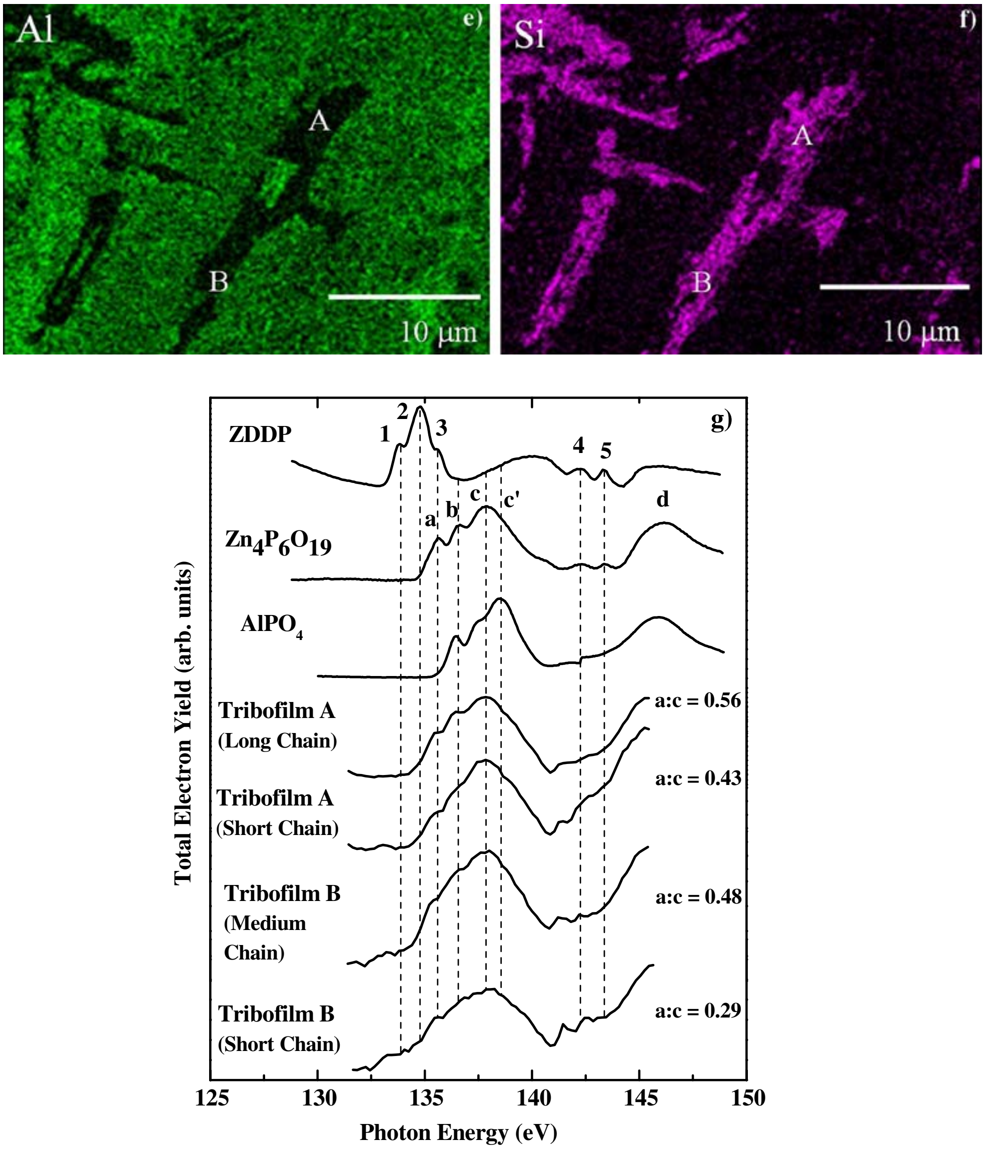

Figure 5. Continued.

distribution of the Si grains. The surface was also chemically etched to expose the Si grains, which ideally act as the load-bearing surface. A390 (16–18% Si) [27] has a different chemical composition but a similar casting procedure was used to prepare it. The Si grain size in A383 lies in between A390 and the Silitec 5 alloy, while the distribution looks very similar to the A390 alloy.

Upon closer inspection of figure 5(a), one finds small patches in the smooth regions and slightly larger patches in the coarser areas. We term these "AW pads", and one can also see streaks elongated in the rubbing direction, similar to previous reports on Al–Si alloys [11,27], and also steel surfaces [16,23,24,26,57,58]. Surrounding those regions labeled A and B are elevated regions of the AW pad. Since the elevated regions are presumably the ones that were in direct contact with the pin, the contact pressures and the frictional forces are dictated only by these elevated regions. The topography of tribofilm B (figure 6(a)) looks similar to that of tribofilm A, although the image appears patchier and more streaks appear in the rubbed direction.

More streaks appear in Nicholls *et al.* [27] AFM images resulting from rubbing, which are not as apparent. We attribute their difference to the higher load (60 N) that was used compared to 40 N used in this study. Different microstructure and composition of the substrate interact differently with the increased pressure.

A number of dynamic factors influence the resulting topography: asperity contact and local pressure, rate of introduction and removal of third bodies, flow of debris, etc. Graham *et al.* [26] used AFM to classify AW pads, and observed wear debris that was not removed by hexane rinsing subsequent to the experiment, or during the AFM contact scan, implying the debris had become incorporated into the film.

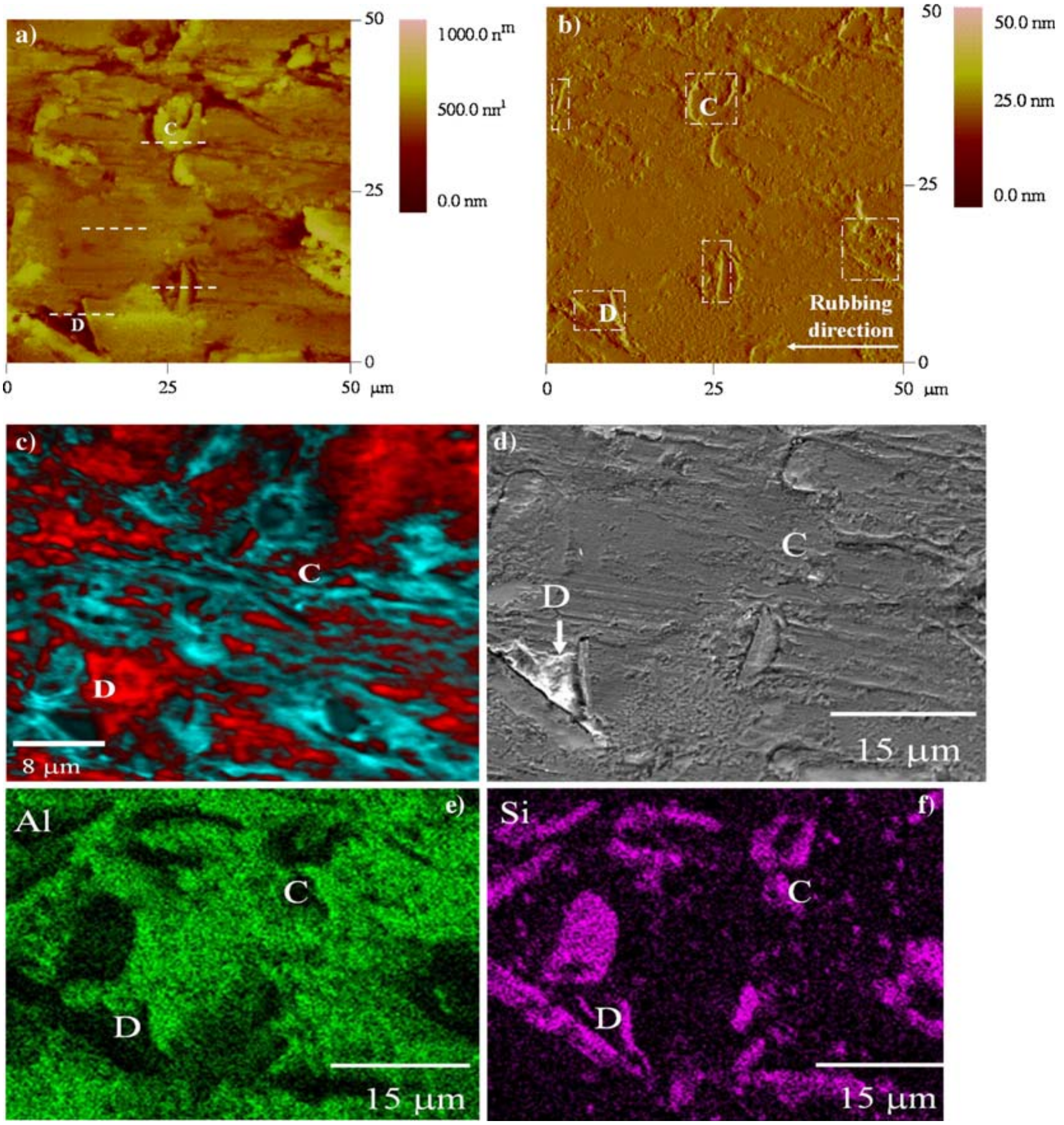

Figure 6. Chemomechanical mapping of tribofilm B. Regions of interest are indicated that can be compared throughout the chemomechanical map. Figure 6(a, b) is 50×50 μm^2 contact AFM height and deflection topography images. The dashed lines and boxes are explained in the text. Figure 6(c) is the X-PEEM distribution map of the region analyzed of tribofilm B. Figure 5(g) shows the corresponding spectra used to generate the distribution map. The red regions indicate medium chain polyphosphates and the cyan areas represent regions of short chain polyphosphates. Black areas are regions where the spectra were not fitted well with neither short nor medium chain polyphosphates. Figure 6(d) A field emission SEM image and figure 6(e, f) mapping EDX of a tribofilm B taken at 5.0 kV and a 17 mm working distance. Brighter areas in the EDX map indicate an abundance of the particular element shown.

Figures 5(c) and 6(c) show X-PEEM distribution maps of tribofilms A and B, obtained using the internal model spectra shown in figure 5(g). Details of the X-PEEM analysis can be found elsewhere [11,23,25,59], but briefly, spectra from pixels or regions of interest in the AW film are compared with model spectra for different chain lengths and assigned a color based upon whether they are characteristic of long or short chain polyphosphates.

Figure 5(g) compares the internal model spectra used from tribofilm A and B (spectra acquired in regions smaller less than 4 μm^2) to model compounds ZDDP, $Zn_4P_6O_{19}$, and $AlPO_4$. The low-energy grating was used to acquire the data, thus the spectra are terminated at ~146 eV. In the four spectra compared, we illustrate a polyphosphate of different chain length. We cannot distinguish the cation, but speculate that since the main peak of the tribofilms (peak c) align very well to the main peaks (peaks a and c) of $Zn_4P_6O_{19}$, that Zn is the most abundant cation present. But, one cannot dismiss the presence of Al in the polyphosphate glass. A small shoulder aligning with peak a of the tribofilms (or peak 2 of ZDDP) indicates the presence of unreacted ZDDP. Unreacted ZDDP was found under all conditions (see P K-edge XANES discussion) in the contact zones. We have suggested [11,27] that the presence of unreacted ZDDP is beneficial to its AW action by acting as a source for formation of 'fresh' polyphosphate films when the original film is worn away.

A linear regression analysis was applied pixel-by-pixel to the acquired image sequence, from which component maps were generated, and regions corresponding to long- (blue) and short-(yellow)chain polyphosphate distribution were constructed for tribofilm A (figure 5(c)). The same procedure was carried out for tribofilm B, using regions corresponding to medium-(red) and short-(cyan)chain polyphosphates (figure 6(c)). Regions whose spectra match quite well to the internal model spectra are colored while black areas in both figures 5(c) and 6(c) indicate the absence of a good fit to either model spectrum. This analysis is only semi-quantitative since the films are probably complex mixtures containing a wide range of chain lengths [60] but the images do capture the overall distribution of long and short chain polyphosphates.

The area analyzed in figure 5(c) is primarily short to medium chain (yellow) polyphosphates (a : c = 0.43), with a few localized regions of long chain (blue) polyphosphates (a : c = 0.56). The area investigated in figure 6(c) appears quite similar with respect to the distribution of short- (cyan) (a : c = 0.29) to medium chain (red) polyphosphates (a : c = 0.48). The regions analyzed as medium chain polyphosphates in figures 5(c) and 6(c) have been estimated at ~85 ± 2% and ~22 ± 4%, respectively.

The X-PEEM data (micro-analysis) indicate that care must be taken when interpreting the result of area averaging techniques such as XANES of large areas (e.g., 2×2 mm^2 in the present case). The macro-analysis deconvolution for tribofilm A shows the a : c ratio to be ~0.44 (medium chain polyphosphates), while the micro-analysis (40×40 μm^2 region) shows two distinct regions of a : c ratios, one ~0.43 (medium chain polyphosphates) and the other ~0.56 (long chain polyphosphates). For tribofilm B, the micro-analysis also shows two distinct regions of a : c ratios, one ~0.48 (medium chain polyphosphates) and the other ~0.29 (short chain polyphosphates), while the macro-analysis deconvolution suggests a 0.29 a : c ratio. This confirms that the macro-analysis is a weighted average of the distribution, as indeed is to be expected.

Field emission SEM images of the regions studied by X-PEEM for the respective tribofilms are shown in figures 5(d) (tribofilm A) and 6(d) (tribofilm B). Both were acquired at 5.0 kV to enhance the surface sensitivity. The corresponding EDX maps for aluminum and silicon taken with the SEM are shown, respectively, in figures 5(e, f) (tribofilm A), and 6(e, f) (tribofilm B). The brighter areas correspond to an abundance of that particular element.

The sampling depths of EDX and X-PEEM are substantially different. The X-PEEM sampling depth is ~2–5 nm, while that of EDX is on the micron scale [61]. As a result, bulk silicon and aluminum are being sampled below the AW film, and certain mapped substrate regions may appear modestly larger than compared to the X-PEEM distribution image. We have estimated the aluminum area coverage for both tribofilms A and B to be 78 ± 3% and 84 ± 4%, respectively.

Interesting correlations can be made (considering tribofilm A first) by comparing figure 5(c), with figure 5(e, f). Long chain polyphosphates are forming preferentially on the Si grains, and short chain polyphosphates are situated on the Al matrix. This was first shown by our group [11]; however, the distribution map on the Silitec 5 alloy was more difficult to interpret, due to the larger number of the smaller Si grains, compared to the A383 alloy. We attribute the poorer contrast of the polyphosphate distribution on the Silitec 5 alloy to two main sources: (i) the etching procedure that originally generated a height gradient related to the Si grains protruding from the matrix and (ii) to the greater amount of wear and debris, due to the higher loads tested, in which the wear scar depth (WSD) was greater than the amount by which the Si grains originally stood proud of the Al matrix [54]. This would have redistributed the AW film over the entire alloy surface.

The micro-chemical analysis of tribofilm B is the first such XPEEM analysis of AW films formed at high temperatures. Comparing figure 6(c) with figure 6(e, f), we demonstrate that at high temperatures, medium chain polyphosphates have formed on the Si grains and short chain polyphosphates form on the Al matrix.

Unfortunately, the low-energy grating of the beamline limited the remaining elements to be collected in second order. Signals acquired at the aluminum and sulfur (70–90 eV), and silicon (90–130 eV) L-edges generally were noisy and too weak to obtain meaningful spectra.

3.3. Focused ion beam (FIB) milling

The dashed lines in figures 5(a) and 6(a) are regions where cross-sectional cuts of the tribofilm were made by FIB milling and that were examined and SEM. SEM observations of the FIB cross-section for tribofilms A and B are presented in figure 7. Direct measurement of the cross-sectional thickness of tribofilm A (figure 7(a)) yields values ranging between 40 and 60 nm. The thickness of tribofilm B (figure 7(b)) was measured to vary between 46 and 60 nm. The film is quite homogeneously distributed in both films. Thus for the first time, we have shown directly that the areal density calculated from the P K-edge XANES coupled with the PIXE technique, as shown in table 3, correlates closely with the thickness estimated from FIB milling. Minfray *et al.* [62] measured a film thickness formed by steel on steel contact using a similar FIB milling technique coupled with transmission electron microscopy (TEM) to be ~50 nm.

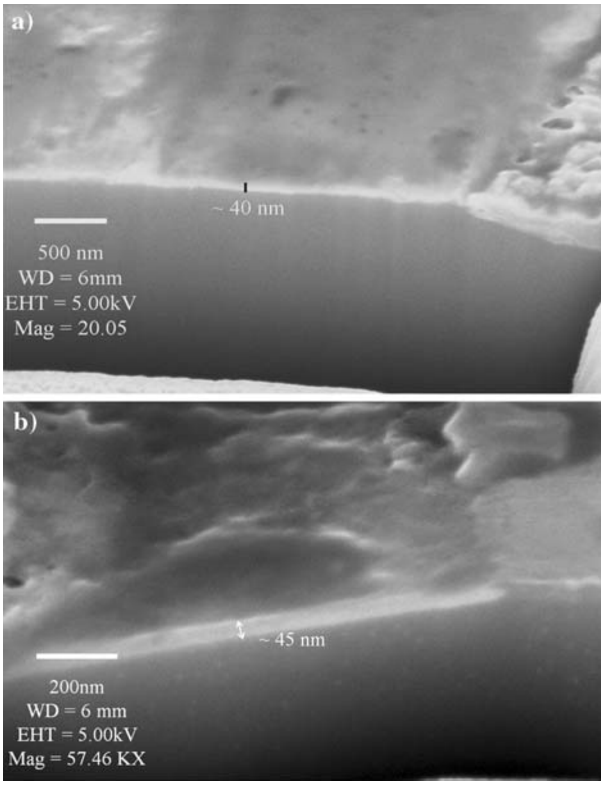

Figure 7. SEM observation of a FIB cross section of (a) Tribofilm A (b) Tribofilm B.

It would be interesting to see if the FIB milled cross sections of the AW films coupled with X-PEEM yield different chemical species, which could be resolved in the Z direction of the film, and push the limits of resolution. This will be attempted in future studies.

3.4. Nanomechanical mapping

Nanoindentation measurements were made on the polished substrate and tribofilms. Details of the instrumentation and calibration have been given elsewhere [23]. Topographic images were taken prior to taking an indent and after indenting a region with the same tip. Force–distance (f–d) curves were taken with loads of 30 μN for the tribofilms, to minimize the influence of the underlying substrate, and to loads of 60 μN for the substrate.

The set-up was calibrated for compliance and abnormalities of the tip, using a succession of indents into fused silica at different penetration depths to calculate the tip area function [27,63]. This function is used in the calculation of the reduced modulus (E^*). The reduced modulus is obtained from the unloading portion of slope from the f–d curve by a method introduced by Oliver and Pharr [48,64,65]. The unloading portion of the f–d curve mimics that of a classic stress–strain curve and, Oliver and Pharr's method assumes E^* is the slope.

Table 3.
Comparing the film thickness using different techniques. P K-edge XANES assumes a uniform polyphosphate with stoichiometry $Zn_2P_2O_7$, and a density of 3.75 g/cm^3.

Tribofilm	P K-edge XANES and PIXE technique (nm)	FIB milling cross section (nm)
Tribofilm A	40 ± 2	40–60
Tribofilm B	42 ± 4	46–60

E^* is related to Young's modulus (E) through equation (2);

$$\frac{1}{E^*} = \frac{\left(1-\upsilon_s^2\right)}{E_s} + \frac{\left(1-\upsilon_i^2\right)}{E_i}, \qquad (2)$$

where E_i and E_s are Young's modulus of the indenter (tip) and sample, and v_i and v_s are the Poisson's ratio of the indenter and sample, respectively. The Young's Modulus (E_s) for the Al matrix and Si grains was found to be 86 ± 4 GPa, and 154 ± 5 GPa, respectively, in good agreement with literature [66,67].

For the tribofilms we generate an indentation moduli (E_s^*), in which the tip properties are removed from the reduced modulus, through the relation (equation 3);

$$E_s^* = \frac{E_s}{\left(1-\upsilon_s^2\right)} = \left[\frac{1}{E^*} - \frac{\left(1-\upsilon_i^2\right)}{E_i}\right]^{-1}. \qquad (3)$$

The indentation moduli are averaged over many indents and the error presented is the standard deviation.

Qualitatively the f–d curves taken on the substrate show that the Si grains are much stiffer and deform less plastically compared to the Al matrix. This is evident from the large hysteresis of the Al matrix curve. The Al curve, shown in figure 8 shows a sudden change in apparent indent depth at fixed load (noted by the arrow), which is caused by the fracturing of the Al oxide layer. The f–d curve in the case of the Si is too narrow to detect any fracturing of the Si oxide layer.

Comparing the f–d curves in figure 8 with figure 9, we observe that the mechanical responses of the AW films are correlated with the underlying substrates. Indentation curves obtained on Si grains show a very high modulus and a very small hysteresis, while the results obtained for the films on the Al matrix resemble the f–d response from the bare Al matrix. Comparing the hysteresis, it is apparent that more plastic deformation has occurred on the AW pad on top of the Si grain compared to the Si grain itself.

The determination of mechanical properties of thin films has become increasingly important because of the applications of such films. There are several methods for partial separation of the elastic modulus of thin films from hard substrates; for a review see Mencik *et al.* [68], which describes five different approximations for evaluating the elastic modulus of the thin films.

The customary way to test the different methods is to use uniform thin films on a uniform substrate, and through successive indentations to different loads,

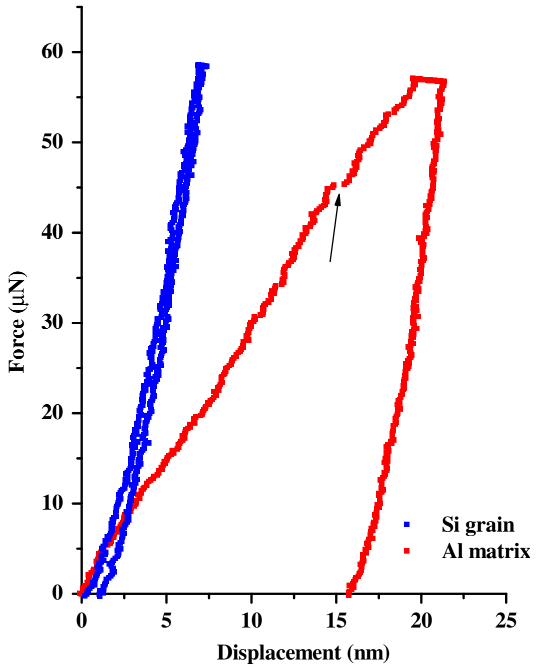

Figure 8. Force–distance (f–d) curves are shown for the polished substrate. F–d curves with a maximum load of 60 μN are shown. The ability to image an area prior to indenting permits the selection of either the Al matrix or Si grain. Dislocations are shown, that are due to fracturing of the aluminum oxide layer (arrow).

empirical fitting parameters can be calculated from regression analysis. Even films as thin as 10 nm have been evaluated [69]. However, a drawback for such techniques is the requirement that composition of the film and substrate must be uniform, in order for the regression analysis to have any significance.

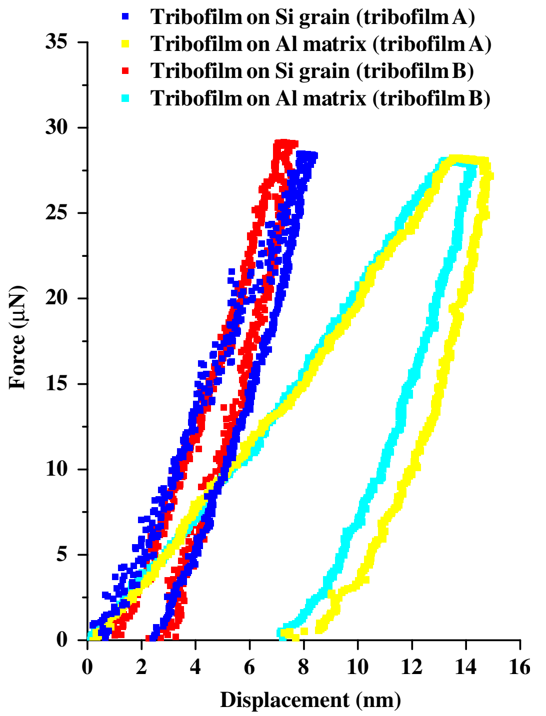

Figure 9. About 30 μN f–d curve obtained on different areas of the tribofilm. Discussion can be found in the text.

We employ a method described by Rar *et al.* [70], that partially separates the indentation modulus of the film from that of the substrate, and which utilizes an analytical solution derived by Gao *et al.* [71], which describes the mechanical behavior of the film through a weighted function, using the following equations;

$$\frac{1}{E_s^*} = \frac{(1 - I_o)}{E_{\text{substrate}}} + \frac{I_o}{E_f}, \tag{4}$$

where E_s* is the indentation modulus of the sample (film and substrate), $E_{\text{substrate}}$ the Young's modulus of the substrate, and E_f is the sought-after separated modulus of the film. The Gao function (I_o), as shown in equation (5), is calculated from the film thickness (t), a Poisson ratio of 0.3 was assumed for each species ($v_{Si} = v_{Al} = v_{\text{film}} = 0.3$), and the films were assumed to be uniform.

$$I_o = \frac{2}{\pi}\arctan\left(\frac{t}{a}\right) + \frac{1}{2\pi(1-\upsilon)} \left[(1-2\upsilon)\frac{t}{a}\ln\frac{1+(t/a)^2}{(t/a)^2} - \frac{(t/a)}{1+(t/a)^2}\right]. \tag{5}$$

The f–d curves taken on the tribofilms show varying E_f values that differ based on indentation location.

Figure 9 shows the indentation curves measured both in and outside of the boxed areas in figures 5(b) and 6(b). Inside the boxed area, we find an E_f value of 84 ± 10 GPa, and 80 ± 13 GPa, respectively, for figures 5(b) and 6(b). The area outside of the boxes in figures 5(b) and 6(b) show an E_f modulus of 44 ± 10 GPa, and 56 ± 12 GPa, respectively, as summarized in table 4.

However, the pads formed on the Si grains are significantly stiffer and less susceptible to plastic deformation than the pads formed on the Al matrix. These findings are well explained by the study of Mosey *et al.*

Table 4.
The indentation moduli (E_s^*), and corrected moduli (E_f) of the AW films formed on tribofilms A and B, presented with other pertinent data to the calculation.

	Film Thickness (nm)	E_f (GPa)[a]
Tribofilm A – Al matrix	40 ± 2	44 ± 10
Tribofilm A – Si grain	40 ± 2	84 ± 10
Tribofilm B – Al matrix	42 ± 4	56 ± 12
Tribofilm B – Si grain	42 ± 4	80 ± 13
Young's modulus		
Al	E_s = 86 ± 4 GPa	
Si	E_s = 154 ± 5 GPa	

[a] I_o was calculated with a Poisson's ratio of 0.3. The corrected modulus was calculated using the film thickness from the P K-edge XANES and was assumed to be uniform and for the Al matrix and Si grains.

[72], in which the authors' calculations show that harder substrates exposed to higher pressures have harder films formed on top of them. Their theory also explains why the film formed on the Al matrix is much softer that the film formed on the Si grains. The small variations in the indentation data between the films on particular substrate features (i.e., on Al matrix, Si grains) are attributed to the differences in topography sampled by the indenter when making an indent, and the difference found between samples are attributed to different formation temperatures used for tribofilms A and B.

The values for the corrected modulus (E_f) of the films formed on the Si grains are higher than observed that in previous work on A390 (~66 ± 7 GPa) [27], although much thicker films were assumed to be formed, and a higher applied load was used (60 N). The indentation moduli found on the Silitec 5 alloy (77 ± 11 GPa) [11], is similar to small AW pads on steel (74 ± 20 GPa) [26], and within the error to the indentation moduli (E_s^*) found in this report for the films on Si grains. There is also a larger deviation from the uncorrected indentation moduli found on the Al matrix on A390 (71 ± 9 GPa) [27], which we believe is attributed to the local roughness and oxide layer thickness both of which influence the modulus in this region.

3.5. *Coefficient of friction (μ) and evaluation of wear*

The coefficient of friction (μ) was measured simultaneously (via the lateral force, F_T) throughout all experiments. In all reported cases, μ increases to a maximum value within less than 5 sec of the onset of the experiment and then drops to a constant level. The initial high-friction value correlates with the lack of a surface film, and once the film has been formed, the friction coefficient decreases and stabilizes. This trend has been observed and described by McQueen *et al.* [35] in a similar experimental set-up studying the friction and wear effects of phosphorus on film formation.

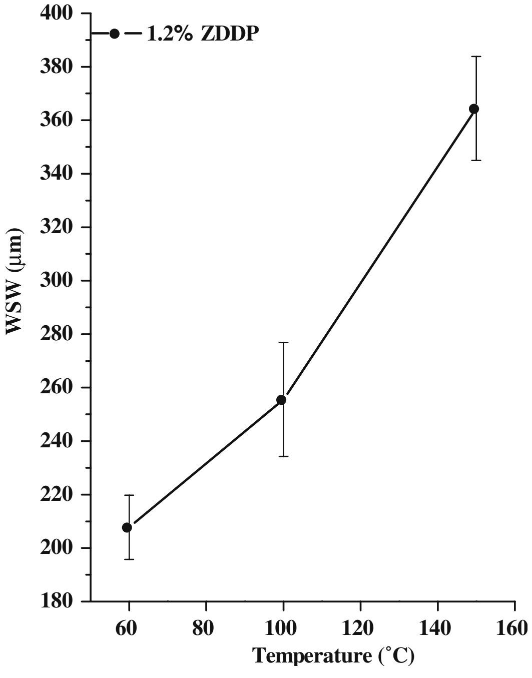

Figure 10. Wear scar with (WSW) comparing temperature of the flat end of the cylindrical 52100 steel pin. Points are an average of 10 or more points along a wear track.

The stabilized value is averaged over many points and that is the value reported. The coefficient of friction (μ) calculated from a normal force (F_N) of 40 N was measured to be 0.13 ± 0.01. This value is typical for the boundary lubrication regime of ZDDP films formed on steel [73].

Presently, we only have a simple method for measuring the wear, as we look at the WSW of the pin after the experiment. Figure 10 presents the WSW as a function of temperature at which the films were formed. From figure 10, it can be seen that the WSW increases almost linearly with temperature.

Nicholls *et al.* [24] using the same 52100 steel composition of pin and coupon under harsher conditions (60 min, 220 N, 100 °C) found a WSW of ~112 μm. In our mildest conditions (5 min, all other conditions were maintained to those of Tribofilm A), the WSW was found to be ~170 μm. This shows that under all our conditions the wear on the pin is larger than using a steel-on-steel couple. Furthermore, Nicholls *et al.* [24] reported having thicker films (68 nm ± 30%) for tribofilms made on steel. In addition, the Al–Si alloy coupons have presumably a larger roughness than the steel coupons, based on a faster deterioration of the Al matrix compared to the Si grains when polishing. We believe that these three variables, WSW, film thickness, and coupon roughness are directly correlated.

4. Summary and conclusions

In this study, we have shown X-PEEM, XANES, and SEM-EDX mapping can be used in tandem to help understand the chemistry of the tribofilms made on A383. In complementary experiments, AFM and SEM reveal the topography and morphology of the films and substrate, while imaging nanoindentation directly and quantitatively measures differences in the mechanical properties of the films. Furthermore, we have shown that P K-edge XANES combined with PIXE is helpful in estimating the film thickness and is in very good agreement with the results obtained for the film thickness with the FIB results.

The following conclusions can be drawn from the results;

1. Large area (macro-scale; 2×2 mm^2) chemical analysis by XANES shows that a polyphosphate glass is

the primary species formed on the surface of A383 after rubbing (under all conditions). The percentage of phosphorous present as polyphosphate was $\sim 83 \pm 7\%$, under most conditions, except the harsher conditions (high temperatures and longer rubbing times), which generated percentages $> 90\%$. The formation of a LI was observed for films generated at higher temperatures, and appeared to be absent at lower temperatures. The macro-scale analysis, indicated that the tribofilm formed at 100 °C (tribofilm A) comprised mostly a short to medium chain polyphosphate. Tribofilm B (formed at 150 °C) comprised mainly short chain polyphosphates. Limitations in our ability to distinguish between aluminum polyphosphates and zinc polyphosphates mean that aluminum ions might be included in the film.
2. Micro-scale (micro-scale; $40 \times 40\ \mu\text{m}^2$) X-PEEM analysis shows a distribution of polyphosphate chain lengths on the surface, which is temperature dependent. At higher temperatures, medium chain phosphates form on the Si grains (shown by the peak ratios a : c $\sim$0.44), while at lower temperatures, longer chain polyphosphates are detected on the Si grains (a : c $\sim$0.56). In both the high temperature and low-temperature study, short chain polyphosphates form on the Al matrix (a : c $<$ 0.44). It is clear that macro-scale analysis by XANES yields an L-edge, which is a weighted distribution of signals from the different areas of the film in the analysis region.
3. FIB used in conjunction with SEM to generate a cross section of an AW film from which the thickness could be directly measured. These data show that the semi-quantitative method of estimating AW film thickness by comparing the P K-edge areal density with samples of known thicknesses is quite reliable.
4. Using the Song and Pharr method with a calculated Gao function, a corrected modulus was obtained which had similar values for the pads on Si grains, but higher than that of similar pads on A390, and softer pads on the Al matrix. The observation of harder and stiffer pads on the Si grains is consistent with recent theoretical calculations.
5. The coefficient of friction was measured to be 0.13 ± 0.01. The wear scar of the pin was found to be correlated to temperature, and even the mildest conditions examined in this study generated more wear compared to harsher conditions with a steel-on-steel couple.

Acknowledgments

The authors would like to thank Mr. Ross Davidson and the rest of the staff at Surface Science Western (SSW) for assistance in acquiring the SEM/EDX data. We are also grateful to Dr. David Munoz-Paniagua for useful discussions regarding nanoindentation, and to Mr. Phil Shaw, Mr. Brian Dalrymple, Mr. Barakat Misk, and Dr. Leighton Coatsworth, all from The University of Western Ontario, and Dr. Todd Simpson from the Nanofabrication Laboratory, also from The University of Western Ontario. We are also obliged to Dr. Franziskus Heigl and Dr. Astrid Jürgensen, from the Canadian Synchrotron Radiation Facility (CSRF), University of Wisconsin, Madison, for their technical support; Imperial Oil of Canada (ESSO) for oil additives; and the National Science Foundation (NSF) for supporting the SRC under grant # DMR-0537588. This work was financially supported by General Motors of Canada Ltd., General Motors R&D center, the National Research Council of Canada (NRC), and the Natural Sciences and Engineering Research Council of Canada (NSERC).

References

[1] L.E. Reuss and C.N. Hughes, SAE Congr. 710150 (1971) 577.
[2] F.J. Kneisler, D.A. Martens and R.W. Midgley, SAE Congr. 710147 (1971) 520.
[3] A.T. Alpas and J. Zhang, Wear 155 (1992) 83.
[4] X.Y. Li and K.N. Tandon, Wear 245 (2000) 148.
[5] Z. Ma, J. Bi, Y. Lu, H. Shen and Y. Gao, Wear 148 (1991) 287.
[6] P.B.N. Bai and S.K. Biswas, ASLE Trans. 29 (1986) 116.
[7] M.A. Nicholls, P.R. Norton, G.M. Bancroft and M. Kasrai, Wear 257 (2004) 311.
[8] C.M. Chen, C.C. Yang and C.G. Chao, Mater. Sci. Eng. A 397 (2005) 178.
[9] M. Fuller, M. Kasrai, J.S. Sheasby, G.M. Bancroft, K. Fyfe and K.H. Tan, Tribol. Lett. 1 (1995) 367.
[10] Y. Wan, L.L. Cao and Q.J. Xue, Tribol. Int. 30 (1997) 767.
[11] G. Pereira, A. Lachenwitzer, M.A. Nicholls, M. Kasrai, P.R. Norton and G. De Stasio, Tribol. Lett. 18 (2004) 411.
[12] H. Spikes, Tribol. Lett. 17 (2004) 469.
[13] M.A. Nicholls, T. Do, P.R. Norton, M. Kasrai and G.M. Bancroft, Tribol. Int. 38 (2005) 15.
[14] A. Barnes, K.D. Bartle and V. Thibon, Tribol. Int. 34 (2001) 389.
[15] A.J. Gellman and N.D. Spencer, Proc. Inst. Mech. Eng. 216 (2002) 443.
[16] O.L. Warren, J.F. Graham, P.R. Norton, J.E. Houston and T.A. Michalske, Tribol. Lett. 4 (1998) 189.
[17] S.M. Hsu and R.S. Gates, Tribol. Int. 38 (2005) 305.
[18] J. Hershberger, O.O. Ajayi and G.R. Fenske, Tribol. Int. 38 (2005) 299.
[19] M. Suominen-Fuller, M. Kasrai and G.M. Bancroft, in: *Chemical Applications of Synchrotron Radiation Part II: X-ray Applications*, T.-K. Sham, ed. (New Jersey, 2002) pp. 10–91.
[20] K.J. Bird and G.D. Galvin, Wear 37 (1976) 143.
[21] H. Spedding and R.C. Watkins, Tribol. Int. February (1982) 9.
[22] S. Jahanmir, J. Tribol. 109 (1987) 577.
[23] M.A. Nicholls, P.R. Norton, G.M. Bancroft, M. Kasrai, T. Do, B.H. Frazer and G. DeStasio, Tribol. Lett. 17 (2003) 205.
[24] M.A. Nicholls, T. Do, P.R. Norton, G.M. Bancroft, M. Kasrai, T.W. Capehart, Y.T. Cheng and T. Perry, Tribol. Lett. 15 (2003) 241.
[25] M.A. Nicholls, G.M. Bancroft, P.R. Norton, M. Kasrai, G. De Stasio, B.H. Frazer and L.M. Wiese, Tribol. Lett. 17 (2004) 245.
[26] J.F. Graham, C. McCague and P.R. Norton, Tribol. Lett. 6 (1999) 149.
[27] M.A. Nicholls, G.M. Bancroft, P.R. Norton, M. Kasrai, G. De Stasio and L.M. Wiese, Tribol. Lett. 18 (2004) 261.

[28] G. De Stasio, M. Capozi, G.F. Lorusso, P.A. Baudat, T.C. Droubay, P. Perfetti, G. Margaritondo and B.P. Tonner, Rev. Sci. Instrum. 69 (1998) 2062.

[29] G. De Stasio, B. Gilbert, B.H. Frazer, K.H. Nealson, P.G. Conrad, V. Livi, M. Labrenz and J.F. Banfield, J. Electron Spectrosc. Relat. Phenomena 114–116 (2001) 997.

[30] S. Günther, B. Kaulich, L. Gregoratti and M. Kiskinova, Prog. Surf. Sci. 70 (2002) 187.

[31] B.H. Frazer, M. Girasole, L.M. Wiese, T. Franz and G. De Stasio, Ultramicroscopy 99 (2004) 87.

[32] G.W. Canning, M.L. Fuller, G.M. Bancroft, M. Kasrai, J.N. Cutler, G. De Stasio and B. Gilbert, Tribol. Lett. 6 (1999) 159.

[33] J. Gao, W.D. Luedtke, D. Gourdon, M. Ruths, J.N. Israelachvili and U. Landman, J. Phys. Chem. B 108 (2004) 3410.

[34] S. Das and S.K. Biswas, Tribol. Lett. 17 (2004) 623.

[35] J.S. McQueen, H. Gao, E.D. Black, A.K. Gangopadhyay and R.K. Jensen, Tribol. Int. 38 (2005) 289.

[36] H. Ji, M.A. Nicholls, P.R. Norton, M. Kasrai, T. Weston Capehart, T.A. Perry and Y.-T. Cheng, Wear 258 (2005) 789.

[37] S.M. Hsu, Langmuir 12 (1996) 4482.

[38] *Aluminum Alloys, Vol. 9* (ASM International, Materials Park, OH 1985).

[39] G.M. Bancroft, Can. Chem. News 44 (1992) 15.

[40] B.X. Yang, F.H. Middleton, B.G. Olsson, G.M. Bancroft, J.M. Chen, T.K. Sham, K. Tan and D.J. Wallace, Rev. Sci. Instrum. 63 (1992) 1355.

[41] M. Najman, M. Kasrai, G.M. Bancroft, B. Frazer and G. De Stasio, Tribol. Lett. 17 (2004) 811.

[42] M. Kasrai, J.R. Brown, G.M. Bancroft, Z. Yin and K.H. Tan, Int. J. Coal Geol. 32 (1996) 107.

[43] M. Kasrai, Z. Yin, G.M. Bancroft and K. Tan, J. Vacuum Sci. Technol. A 11 (1993) 2694.

[44] B.H. Frazer, B. Gilbert, B.R. Sonderegger and G. De Stasio, Surf. Sci. 537 (2003) 161.

[45] M. Kasrai, W.N. Lennard, R.W. Brunner, G.M. Bancroft, J.A. Bardwell and K.H. Tan, Appl. Surf. Sci. 99 (1996) 303.

[46] C. Jacobsen, S. Wirick, G. Flynn and C. Zimba, J. Microsc. 197 (2000) 173.

[47] L.M. Croll, J.F. Britten, C. Morin, A.P. Hitchcock and H.D.H. Stoever, J. Synchrotron Radiat. 10 (2003) 265.

[48] W.C. Oliver and G.M. Pharr, J. Mater. Res. 7 (1992) 1564.

[49] G.M. Bancroft, M. Kasrai, M. Fuller, Z. Yin, K. Fyfe and K.H. Tan, Tribol. Lett. 3 (1997) 47.

[50] M.L. Suominen-Fuller, M. Kasrai, G.M. Bancroft, K. Fyfe and K.H. Tan, Tribol. Int. 31 (1998) 627.

[51] Z. Yin, M. Kasrai, M. Fuller, G.M. Bancroft, K. Fyfe and K.H. Tan, Wear 202 (1997) 172.

[52] Z. Yin, M. Kasrai, G.M. Bancroft, K.H. Tan and X. Feng, Phys. Rev. B 51 (1995) 742.

[53] D.G.J. Sutherland, M. Kasrai, G.M. Bancroft, Z.F. Liu and K.H. Tan, Phys. Rev. B 48 (1993) 14989.

[54] G. Pereira, A. Lachenwitzer, M.A. Nicholls, M. Kasrai, P.R. Norton and G. De Stasio, Tribol. Lett. 18 (2005) 411.

[55] S.H. Choa, K.C. Ludema, G.E. Potter, B.M. DeKoven, T.A. Morgan and K.K. Kar, Wear 177 (1994) 33.

[56] M.L. Suominen-Fuller, L.R. Fernandez, G.R. Massoumi, W.N. Lennard and M. Kasrai, Tribol. Lett. 8 (2000) 187.

[57] A.J. Pidduck and G.C. Smith, Wear 212 (1997) 254.

[58] A. Tonck, S. Bec, J.M. Georges, R.C. Coy, J.C. Bell and G.W. Roper, Tribol. Ser. 36 (1999) 39.

[59] M.A. Nicholls, G.M. Bancroft, M. Kasrai, P.R. Norton, B.H. Frazer and G. De Stasio, Tribol. Lett. 18 (2004) 453.

[60] I.N. Koprinarov, A.P. Hitchcock, C.T. McCrory and R.F. Childs, J. Phys. Chem. B 106 (2002) 5358.

[61] D. Shindo, T. Oikawa, in: *Analytical Electron Microscopy for Materials Science* (Springer-Verlag, Tokyo, 2002) p. Ch 4.

[62] C. Minfray, J.M. Martin, C. Esnouf, T. Le Mongne, R. Kersting and B. Hagenhoff, Thin Solid Films 447–448 (2004) 272.

[63] M.F. Doerner and W.D. Nix, J. Mater. Res. 1 (1986) 601.

[64] G.M. Pharr and W.C. Oliver, MRS Bullet. 17 (1992) 28.

[65] W.C. Oliver and G.M. Pharr, J. Mater. Res. 19 (2004) 3.

[66] P.J. Blau, in: *ASM Handbook*, Vol. 18, S. Henry, ed. (The Materials Information Society, Materials Park, OH, 1992) pp. 414.

[67] H.A. Schaeffer, in: *Encyclopedia of Materials Science and Engineering*, Vol. 6, M. B. Bever, ed. (Pergamon Press, Oxford, England, 1986).

[68] J. Mencik, D. Munz, E. Quandt, E.R. Weppelmann and M.V. Swain, J. Mater. Res. 12 (1997) 2475.

[69] T. Sawa, Y. Akiyama, A. Shimamoto and K. Tanaka, J. Mater. Res. 14 (1999) 2228.

[70] A. Rar, H. Song and G.M. Pharr, Mater. Res. Soc. Symp. Proc. 695 (2002) 431.

[71] H. Gao, C.-H. Chiu and J. Lee, Int. J. Solids Struct. 29 (1992) 2471.

[72] N.J. Mosey, M.H. Müser and T.K. Woo, Science 307 (2005) 1612.

[73] C. Grossiord, J.M. Martin, T. Le Mogne and T. Palermo, Tribol. Lett. 6 (1999) 171.